The role of high cholesterol in SARS-CoV-2 infectivity

Hao Wang[1,2,3], Zixuan Yuan[1,2,3], Mahmud Arif Pavel[1,2], Sonia Mediouni Jablonski[4], Joseph Jablonski[4], Robert Hobson[5,6], Susana Valente[4], Chakravarthy B. Reddy[7], and Scott B. Hansen[1,2,*]

From the [1]Department of Molecular Medicine, [2]Department of Neuroscience, [3]Skaggs Graduate School of Chemical and Biological Sciences, and [4]Department of Immunology and Virology, The Scripps Research Institute, Jupiter, Florida, USA; [5]Bruker Nano Surfaces, Fitchburg, Wisconsin, USA; [6]Department of Biology, University of Utah, Salt Lake City, Utah, USA; [7]Department of Internal Medicine, University of Utah Health Sciences Center, Salt Lake City, Utah, USA

Coronavirus disease 2019 (COVID-19) is a respiratory infection caused by severe acute respiratory syndrome coronavirus 2. The virus binds to angiotensinogen converting enzyme 2 (ACE2), which mediates viral entry into mammalian cells. COVID-19 is notably severe in the elderly and in those with underlying chronic conditions. The cause of selective severity is not well understood. Here we show cholesterol and the signaling lipid phosphatidyl-inositol 4,5 bisphosphate (PIP$_2$) regulate viral infectivity through the localization of ACE2's into nanoscopic (<200 nm) lipid clusters. Uptake of cholesterol into cell membranes (a condition common to chronic disease) causes ACE2 to move from PIP$_2$ lipids to endocytic ganglioside (GM1) lipids, where the virus is optimally located for viral entry. In mice, age and high-fat diet increase lung tissue cholesterol by up to 40%. And in smokers with chronic disease, cholesterol is elevated 2-fold, a magnitude of change that dramatically increases infectivity of virus in cell culture. We conclude increasing the ACE2 location near endocytic lipids increases viral infectivity and may help explain the selective severity of COVID-19 in aged and diseased populations.

Early in the coronavirus disease 2019 (COVID-19) pandemic, the lethality of severe acute respiratory syndrome coronavirus 2 (SARS-CoV-2) was notably selective for the elderly (1, 2) and those with chronic diseases such as hypertension, diabetes, and Alzheimer's and cardiovascular diseases (3–5). Interestingly, most children presented with very minor symptoms, while the elderly and those with underlying conditions experienced very severe life-threatening symptoms leading to much higher death rates (6).

SARS-CoV-2 attaches to the cell surface by binding to a receptor, angiotensinogen converting enzyme 2 (ACE2) (7, 8). After binding, SARS-CoV-2 is thought to enter the cells through either a cell surface mechanism that involves transmembrane protease, serine 2 (TMPRSS2) enzyme (9–11) or endocytosis, a cholesterol-dependent mechanism that involves monosialotetrahexosylganglioside1 (GM1)-containing lipid

clusters (12–16). The cholesterol orders the GM1 lipids creating a structured binding site with high affinity for palmitates covalently attached to the ACE2 protein (Fig. S1A) (17, 18). Recent data suggest the endocytic pathway plays a more prominent role in viral entry than previously thought (19, 20). Interestingly, the more recent omicron variant, which is more infectious (21, 22), enters predominantly through the endocytic pathway, TMPRSS2 (19, 20, 23).

Understanding cholesterol regulation in SARS-CoV-2 entrance into the endocytic pathway appears important for understanding the virus's infectivity. Compounds that disrupt ACE2 association with GM1 lipids decreases entrance into the endocytic pathway, which also decreases infectivity (17). Understanding the effect of age and chronic disease on cholesterol could help explain the selectivity of the alpha variant and how more recent variants have evolved to increase infectivity.

One function of cellular cholesterol is to cluster membrane proteins (24). In biological membranes, cholesterol-regulated proteins (*e.g.*, ACE2) can move between GM1 clusters and PIP$_2$ clusters in response to changing cholesterol levels, while other, cholesterol-independent proteins, remain clustered with GM1 lipids (*e.g.*, β- and γ-secretase). The movement of select proteins between GM1 and PIP$_2$ can facilitate substrate presentation, a process that activates an enzyme (17, 18, 25–28).

Cholesterol-dependent clustering in GM1 lipids can increase viral entry (15, 17, 29, 30). Previous experiments showed ACE2 associated with detergent-resistant membranes (14, 31), which are similar in composition to GM1 clusters. ACE2 also associates with PIP$_2$ clusters and moves between the two domains (17, 32). We hypothesized that cholesterol regulates the ACE2 receptor's entrance into the endocytic pathway by moving between the GM1 and PIP$_2$ clusters. Here we show uptake of cholesterol into tissue regulates ACE2 nanoscopic location and its association with endocytic lipids.

Results and discussion

Regulation of ACE2 movement between GM1 and PIP$_2$ clusters by cholesterol

To monitor nanoscopic movement of ACE2 to GM1 clusters, we colabeled ACE2 and GM1 clusters in human embryonic kidney 293T (HEK293T), treated cells with apolipoprotein E (apoE) with and without cholesterol (± Chol), and imaged with

---

* For correspondence: Scott B. Hansen, shansen@scripps.edu.

direct stochastic optical reconstruction microscopy (dSTORM). ACE2 antibody was previously validated by Western blot (see Experimental procedures), and Gm1 lipids were labeled with cholera toxin B (CTxB). dSTORM and other superresolution techniques are capable of visualizing nanoscale arrangements (*i.e.*, sub-100-nm-diameter lipid structures) in intact cellular membranes (33–35).

ApoE is a cholesterol transport protein whose regulation is receptor mediated (36). In the blood, cholesterol uptake is associated with inflammatory lipids and their uptake induces inflammation (37). The uptake is mediated by low-density lipoprotein receptor, which selectively binds to the lipidated form of apoE (36). We used lipidated apoE as a physiologically relevant tool to facilitate cholesterol uptake into the cell (Fig. S1*B*). We lipidated apoE, with 10% fetal bovine serum (FBS). Since it is a natural source, the treatments include the mixture of lipids normally associated with apoE-mediated uptake. Importantly, apoE is not present in FBS, allowing us to carefully control the amount of uptake (38).

Nonlipidated apoE binds selectively to the very low-density lipoprotein receptor. Cells releasing nonlipidated apoE

facilitate cholesterol efflux and decrease inflammation (37, 39). Here we use nonlipidated apoE to induce a noninflammatory state of the cells. Nonlipidated apoE effluxes cholesterol from cells (17, 28, 39, 40). This allows us to trap cells in physiologically relevant states prior to superresolution imaging. Furthermore, the apoE 4 isotype (apoE4) was recently linked to severity of COVID-19 (41). ApoE4 is also known as the most prevalent genetic marker of sporadic Alzheimer's disease (28).

Figure 1*A* shows representative dSTORM images of ACE2 and GM1 clusters from apoE-treated HEK293T cells (± Chol) (Fig. 2*A*). The association of ACE2 with GM1 clusters was measured by pair correlation (25, 26, 28, 42). We used endogenous ACE2 expression in HEK293 (17, 23, 43) to avoid nonphysiological levels of ACE2 and artifacts that may arise due to overexpression of the protein (23).

We found pair correlation of ACE2 with GM1 clusters increased more than 3-fold with lipidated apoE (inflamed state) (Fig. 1*B*). The increased correlation was not due to a change in ACE2 concentration on the cell surface (Fig. S2, *A* and *B*). As a positive control, and to confirm that the effect depends on cholesterol and not another component of the
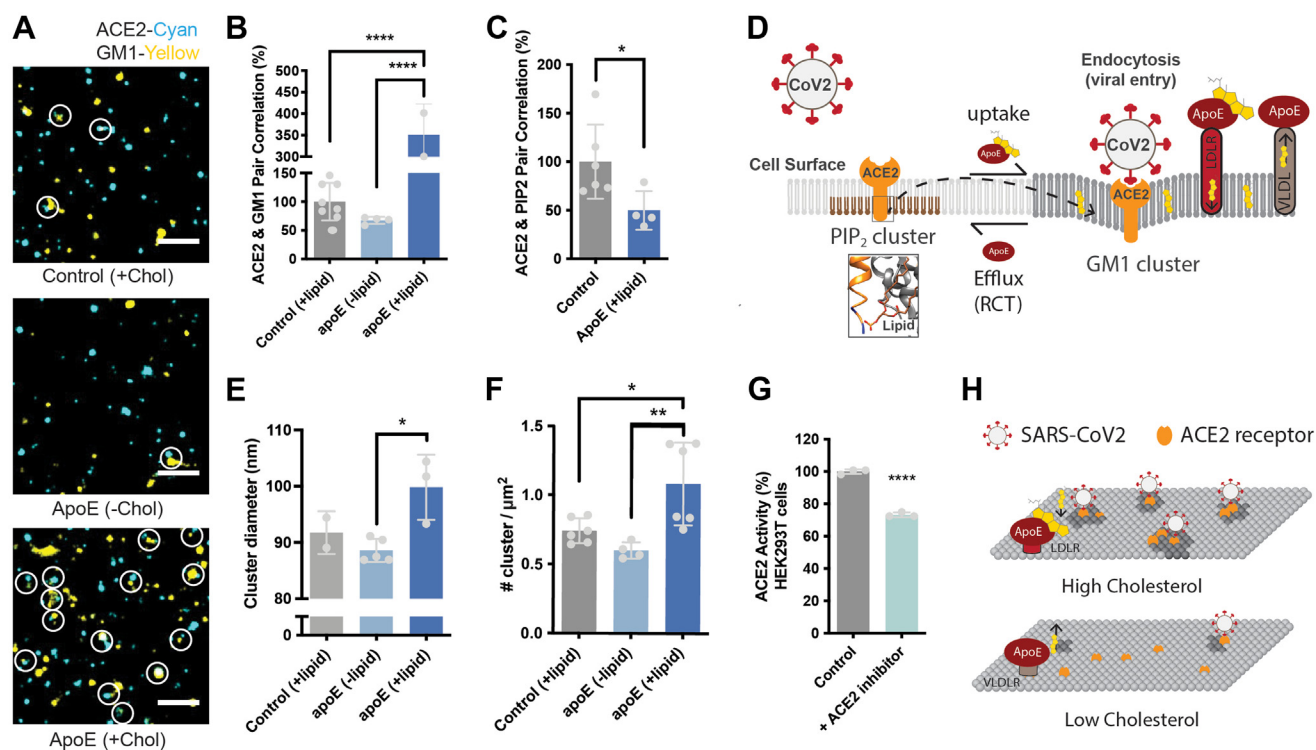

Figure 1. ApoE lipids shift ACE2 to an endocytic pathway. *A*, representative images from dSTORM superresolution imaging. GM1 clusters (*yellow*) increase dramatically in the presence of blood serum when apoE is present (*bottom panel*), labeled with CTxB. ACE2 receptor (*cyan*) labeled with ACE2 antibody has very little overlap (*white circle*) with GM1 clusters when blood serum is removed (*middle panel*). The scale bar represents 1 μm. *B* and *C*, pair correlation from dSTORM imaging. ACE2 was compared with GM1 lipids (CTxB labeled, *B*) and phosphatidyl inositol 4,5-bisphosphate (PIP$_2$, *C*). Loading cells with lipidated apoE (+chol) (*dark blue* shading) increased the pair correlation with GM1 clusters and decreased the pair correlation with PIP$_2$ clusters. Hence apoE-mediated lipid influx moves ACE2 from PIP$_2$ clusters to GM1 clusters. *D*, model showing cholesterol-dependent cluster-associated protein activation of ACE2 from PIP$_2$ domains (*brown* lipids) to endocytic GM1 lipids (*dark gray*) and enhanced SARS-CoV-2 viral entry. Lipidated apoE is shown bound to low-density lipoprotein receptor (LDLR) (*red*) and delipidated apoE is shown bound to very low-density lipoprotein receptor (VLDLR). VLDLR facilitates reverse cholesterol transport (RCT). An inset shows the cryo-EM structure (PDB 6M18) of an anionic lipid-binding site (putative PIP$_2$ site) in ACE2. See also supporting information. *E*, cluster size analysis suggests GM1 clustering is regulated by apoE-mediated lipid transportation between serum and cell membrane. *F*, ApoE transportation of lipid regulates apparent cluster density. Cholesterol influx from serum results in an increase in number and apparent size. *G*, ACE2 activity assay was performed to detect ACE2's expression in wildtype HEK293T cells. Cells incubated with ACE2 inhibitor showed significantly decreased ACE2 activity, suggesting ACE2 is expressed in the HEK293T cells. Data are expressed as mean ± SD, *$p < 0.05$, **$p < 0.01$, ****$p < 0.0001$, two-sided Student's *t* test. *H*, model for SARS-CoV-2 viral entry in high and low cholesterol. When cholesterol is high, ACE2 translocated to GM1 clusters, a position optimal for viral binding and endocytosis. When cholesterol is low, ACE2 traffics away from GM1 clusters, a position that poorly facilitates viral infection (PIP$_2$ domains not shown).
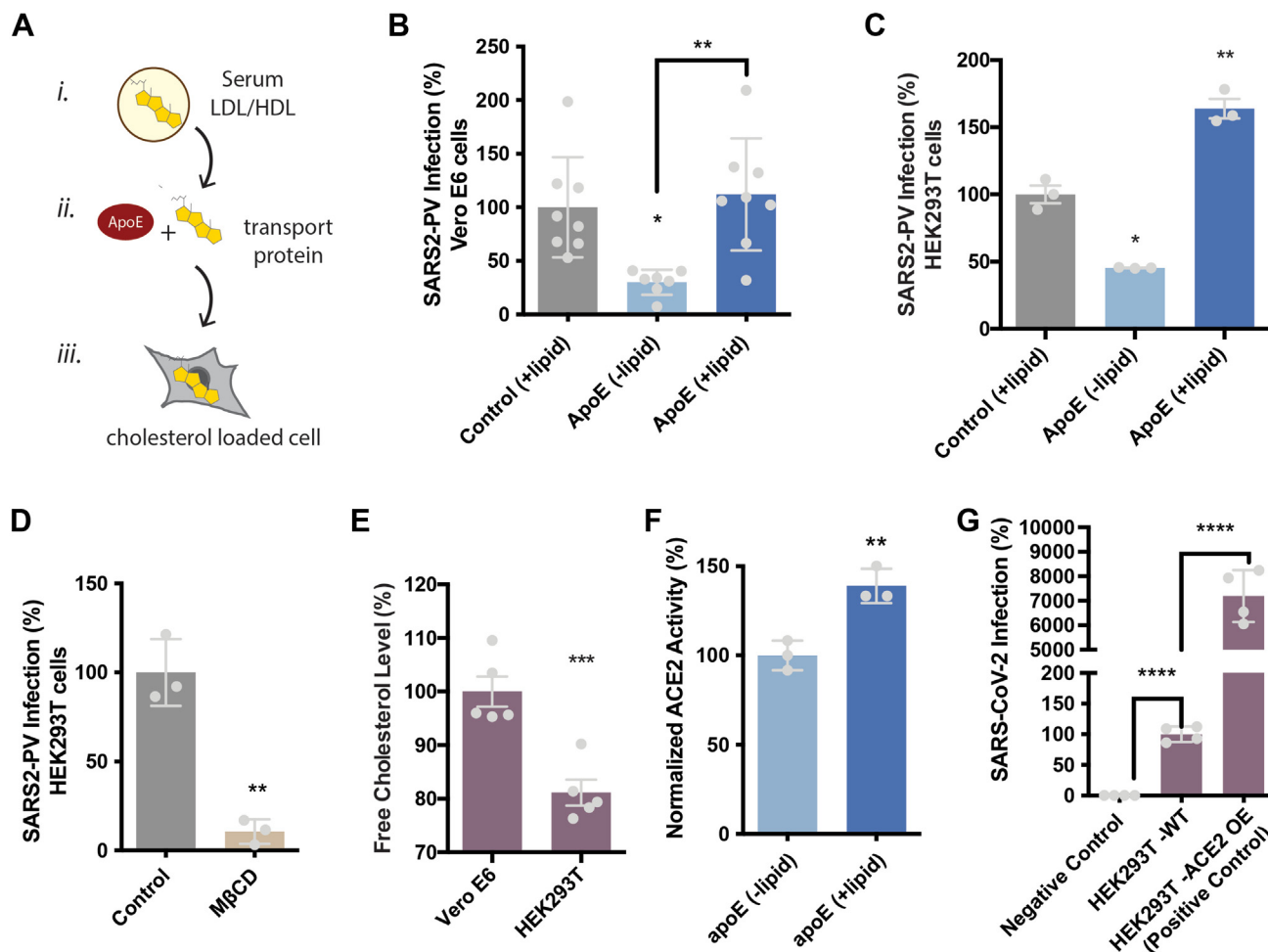
Figure 2. Serum lipids increase SARS-CoV-2 pseudovirus (SARS2-PV) infection. *A*, cartoon diagram showing the experimental setup for loading cultured cells with cholesterol and saturated lipids. *i.*, cholesterol (*yellow* shading) loaded into lipoprotein (*e.g.*, low- and high-density lipoprotein [LDL and HDL, respectively]) from blood serum. *ii.*, delipidated human apolipoprotein E (apoE), a cholesterol transport protein, is exposed to cholesterol from blood serum, and *iii*, ApoE transports cholesterol into cells (*gray* shading) (see also Fig. S1*B*). B and C, SARS-CoV-2 pseudovirus (SARS2-PV) entry assay in VeroE6 cells (*B*) and HEK293T cells (*C*). Cells were treated with a luciferase expressing retrovirus pseudotyped with the SARS-CoV-2 spike protein that recapitulates viral entry. Infectivity was monitored by a luciferase activity in cells treated with or without apoE. Viral infection in cells with high cholesterol (apoE + serum) was more than 3-fold higher compared with that in cells with low cholesterol. Data are expressed as mean ± SD, *$p < 0.05$, **$p < 0.01$, one-way ANOVA. *D*, depletion of cellular cholesterol with methyl-beta-cyclodextrin (MβCD) blocked almost all viral entry measured by pseudotyped luciferase assay. Data are expressed as mean ± SD, **$p < 0.01$, two-sided Student's *t* test. *E*, free cholesterol level is higher in VeroE6 cells than in HEK293T cells. Data are expressed as mean ± SD, ***$p < 0.001$, two-sided Student's *t* test. *F*, ACE2's enzymatic activity is regulated by membrane cholesterol. ApoE-mediated cholesterol depletion from cell membrane inhibits ACE2's activity. Data are expressed as mean ± SD, *$p < 0.05$, **$p < 0.01$, ****$p < 0.0001$, one-way ANOVA. *G*, SARS2-PV viral entry with wildtype (WT) HEK293T expressing endogenous ACE2 and HEK293T overexpressing hACE2 (ACE2 OE). Negative control is HEK293T cells treated identical to the other conditions except no virus was applied. The endogenous expression was low but presumably much more physiologically relevant and shows ACE2 is expressed in HEK293T sells albeit at comparatively low quantities. The result is a single side-by-side comparison, but the values are in a typical range we see for these two systems. Data are expressed as mean ± SD, ****$p < 0.0001$, one-way ANOVA.

serum or apoE regulation, we treated the cells with methyl-β-cyclodextrin (MβCD), a chemical known to extract cholesterol from the plasma membrane. MβCD reduced ACE2's pair correlation with endocytic lipids by ∼70% (Fig. S2*C*).

We then colabeled ACE2 with PIP$_2$ lipids. As mentioned, PIP$_2$ is a polyunsaturated lipid that forms cholesterol-independent domains (44) away from GM1 clusters (26, 44–46) (Fig. S1*A*). As expected, changes in ACE2–PIP$_2$ pair correlation were opposite of ACE2–GM1. Lipidated apoE decreased ACE2's association with PIP$_2$ (Fig. 1*C*). These data suggest that cholesterol-induced clustering moves ACE2 from PIP$_2$ clusters to GM1 clusters (Fig. 1*D*). Owing to the nature of dSTORM, the changes in pair correlation are relative shifts;

they are not quantitative of the amount of protein at each location.

We next investigated the effect of lipidated apoE uptake on the number and size of endocytic lipids in plasma membrane. Using cluster analysis, we found cholesterol-loaded cells increased in both the number and apparent diameter of GM1 clusters compared with control (Fig. 1, *E*, *F* and *H*). Cholesterol depletion by MβCD decreases the apparent cluster size (Fig. S2*D*). These decreases caused GM1 clusters to separate from each other measured by Ripley's H function (Fig. S2*E*). The cells were fixed prior to labeling to reduce potential artifacts in their size due to CTxB clustering (47) (see discussion).

High cholesterol in SARS-CoV-2 infectivity

To verify the presence of endogenously expressed ACE2 in wildtype (WT) HEK293T cells, we measured ACE2 activity using a fluorescent substrate cleavage assay. The ACE2-specific inhibitor DX600 (0.88 mM) decreased fluorescence by 30% compared with control (Fig. 1G) suggesting that ACE2 is present, and this result is consistent with that of others who measured ACE2 in cultured cells (17, 23, 43). The inhibition was not 100%, presumably from additional enzymes in the lysate that cut the substrate we used. We also measured ACE2 activity in cholesterol-loaded and depleted cells. We found ACE2 activity in HEK293T cells decreased by ∼40% after cholesterol depletion, and cholesterol loading compensated for the decrease (Fig. 2F), again confirming the observation that ACE2 is endogenously expressed in HEK293T (23, 43).

Effects of ACE2 localization on SARS-CoV-2 pseudovirus entry

To confirm the movement of ACE2 to GM1 lipids increases endocytosis, we infected lipid-loaded (inflammatory) VeroE6 and HEK293T cells with pseudotyped SARS-CoV-2 (SARS2-PV). SARS-CoV-2 efficiently infects VeroE6 (48).

We found cholesterol extraction from the membrane with apoE (apoE-Chol) decreased SARS2-PV entry into both VeroE6 and WT HEK293T cells by ∼50% (Fig. 2, B and C). MβCD inhibited SARS2-PV entry by over 90% (Fig. 2D). The cells were pretreated with apoE (± Chol), so the virion did not experience any cholesterol treatment, only the cells. Cholesterol in the virion can also affect viral entry (49) which we do not address here.

Treating HEK293T cells with lipidated apoE (apoE+Chol) had the opposite effect as depletion—the infectivity of cholesterol-loaded cells was 50% greater compared with control cells without apoE treatment, and 3-fold greater than cells treated with delipidated apoE (apoE-Chol). Viral infectivity of VeroE6 cells was also significantly higher in high cholesterol compared with low cholesterol condition. In control experiments, WT HEK293T cells were infected about 70-fold lower than the same HEK293T cells overexpressing ACE2 (Fig. 2G).

To confirm our apoE treatment increases the membrane cholesterol of VeroE6 and HEK293T cells, we performed a fluorometric cholesterol assay using cholesterol oxidase. We found that free cholesterol (FC) level was ∼20% higher in VeroE6 compared with HEK293T (Fig. 2E). In contrast, the total cholesterol level was about the same in the two cell lines (Fig. S3C), suggesting VeroE6 cells are regulated to have more cholesterol in the plasma membrane.

As mentioned, many viruses are regulated by cholesterol. To determine if SARS-CoV-2 is particularly sensitive to cholesterol, we compared it with vesiculovirus, a genetically unrelated virus that also enters through a cholesterol-dependent pathway. Pseudotyped vesiculovirus (VSV-G) was less sensitive to cholesterol compared with SARS2-PV, although a similar trend was visible, as expected for a cholesterol-dependent pathway (Fig. S3A). Likewise, cholesterol modulation with MβCD had a much less effect on VSV-G viral entry compared with SARS-CoV-2 (Fig. S3B), confirming that SARS-CoV-2 is particularly sensitive to cholesterol.

Cholesterol uptake and ACE2 localization in mouse lung tissue

Next, we asked if age and disease could affect the cellular cholesterol and, if so, does it affect the location of ACE2 in GM1 lipids? To determine whether there is an age-dependent effect on tissue cholesterol, we measured cholesterol levels in lungs from young (8-week-old) and aged (28-week-old) C57BL/6J mice. We found age elevated cholesterol in the lung of old mice ∼45% compared with young mice (Fig. 3, A and B).

Next, we investigated cholesterol levels in lung tissue of diabetic 28-week-old C57B/6J mice. Diet-induced obesity (DIO) is a well-established model for type II diabetes (50). Normalized cholesterol level was significantly elevated in DIO mice compared with both 8-week-old and 28-week-old healthy mice (40% and 22%, respectively), suggesting an age- and obesity-induced sensitivity to viral infection exists *in vivo*. We normalized the amount of cholesterol to total protein in the tissue homogenate to control for potential excess water in the diabetic lung (Fig. S3D). Lung cholesterol was 0.24 ± 0.06 μg/mg wet tissue (Fig. S3E). To further confirm a cholesterol-dependent effect, we tested ACE2 localization to GM1 clusters in lung slices from obese mice using dSTORM pair correlation. The percent pair correlation was more than an order of magnitude higher in lungs from obese mice compared with either young or aged healthy animals (Fig. 3, C–E). There appeared to be two populations. The reason is likely due to a population of cells that does not respond. ACE2 signal in lung tissue was sparser than in cultured cells (Fig. 3E), likely contributing to some variability. Figure 3F shows an ACE2-based model for age- and disease-related SARS-CoV-2 infectivity based on the cholesterol data and our ACE2 trafficking in mouse lung and cell culture. In aged obese mice, ACE2 shifts to the GM1 clusters and facilitates viral infection through endocytosis.

Endogenous cholesterol levels in human tissue and cultured cells

To directly compare cholesterol in whole lung tissue with cell culture and to better compare samples of known high infectivity with those of low infectivity, we examined cholesterol levels in smoker's lung tissue and cultured lung cells A549 and H1793. Human lungs are susceptible to infection, especially smokers' lungs, while cultured lung cells are relatively resistant (17). We found that cultured cells had 50 to 70% less FC compared with lung tissue from smokers (Fig. 4A). VeroE6 cells had the most cholesterol among cultured cells but less than human lung tissue. Interestingly, total cholesterol (FC + cholesteryl esters) was roughly the same (Fig. S3C) for VeroE6 and HEK293T, suggesting the difference is in the FC. FC is typically in the plasma membrane, whereas cholesteryl esters are more prominent in internal stores (49, 51, 52).

We reasoned that cholesterol could change the cluster size of endocytic lipids. We found VeroE6 had large GM1 clusters, almost twice that of HEK293T cells (Fig. 4B). These results suggest that, although the total cholesterol level in HEK293T and VeroE6 are relatively similar, the free cholesterol in the plasma membrane appears more abundant in Vero E6 cells.
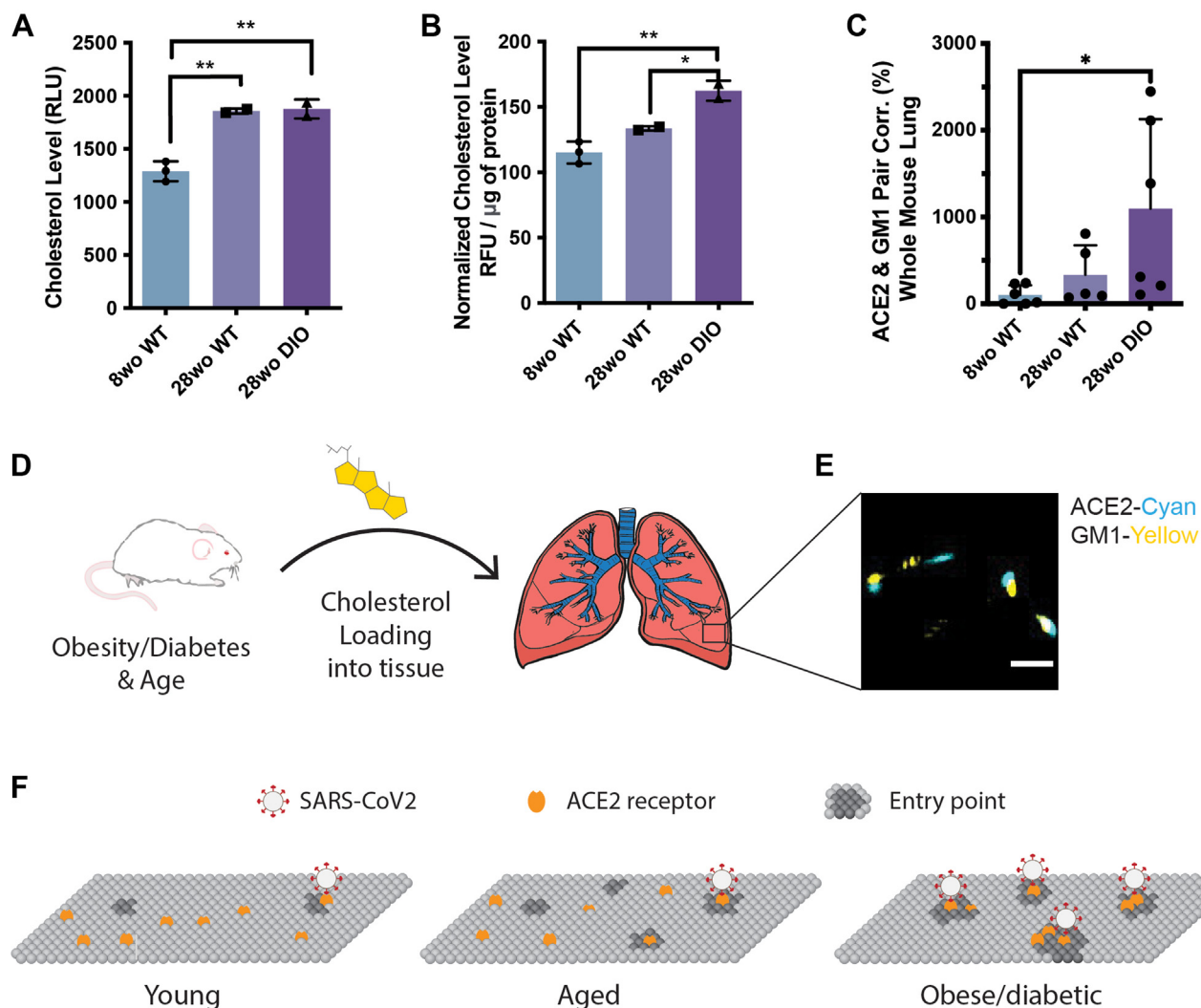
Figure 3. Age and disease increase cholesterol in mouse lung tissue. *A* and *B*, cholesterol measured per milligram of lung tissue (*A*) and per microgram of total proteins in the lung (*B*) in 8-week-old (wo) and 28wo mice. An aged diabetic mouse, generated by diet induced obesity (DIO), loaded ~45% more cholesterol into its lung tissue per microgram of total proteins. *C*, association of ACE2 with GM1 clusters determined by dSTORM pair correlation in mouse lung tissue. Data are expressed as mean ± SD., *$p < 0.05$, **$p < 0.01$, one-way ANOVA). *D*, cholesterol is taken up into the lung tissue of mice fed a high-fat diet. *E*, representative dSTORM images from (*C*). Cholesterol (*yellow* shading) was loaded into the lung of mice (*left*) and fixed and removed and the tissue directly imaged. The scale bar represents 500 nm. *F*, proposed model for SARS-CoV-2 infection in obese patients. In young individuals, cholesterol level is low, there are few GM1 clusters (*dark gray*, entry points), and ACE2 traffics to disordered lipids ~50 nm away from GM1 clusters (endocytic lipids). With age, average cholesterol levels in the tissue increases. In obese/diabetic patients, tissue cholesterol levels are the highest and ACE2 receptor is positioned in GM1 clusters for optimal viral entry (PIP$_2$ domains not shown).

As mentioned, overexpression of ACE2 renders HEK293T cells highly susceptible to infection. We found infection increased ~70 times higher (Fig. 2*G*) compared with WT HEK293T. To test the potential role of ACE2 expression in SARS-CoV-2 infectivity, we compared ACE2 protein levels in lung tissue of smokers with the various cell lines using an ELISA assay for ACE2 protein. We found endogenous ACE2 protein levels in HEK293T were approximately the same as in human lung and veroE6, which are easily infected (Fig. 4*C*). This suggests the ACE2 protein levels are not the primary driver of infectivity in cells with endogenous ACE2 and normal to high levels of cholesterol.

Conclusion

Taken together, our findings show that cholesterol in the plasma membrane is an important regulator of ACE2 localization between GM1 and PIP$_2$ clusters and this distribution is a core contributor to SARS-CoV-2 entering the endocytic pathway. Additional saturated lipids, such as sphingomyelins, which are minor components of apoE cargo, likely contribute to ACE2 translocation especially in the aged and those with chronic inflammation.

Why the omicron variant is more sensitive to the endocytic pathway is unclear. The omicron receptor-binding domain has higher affinity for ACE2 (53–55). Our data suggest the ACE2 receptor is mobile (Fig. 1, *A–D*), hence the higher affinity of the omicron spike protein for ACE2 could increase the probability of viral binding when ACE2 moves near endocytic lipids. This would be most notable in individuals with low cholesterol where the receptor spends more time near PIP$_2$ clusters compared with the GM1. In individuals with high cholesterol ACE2 would spend more time in GM1 lipids and
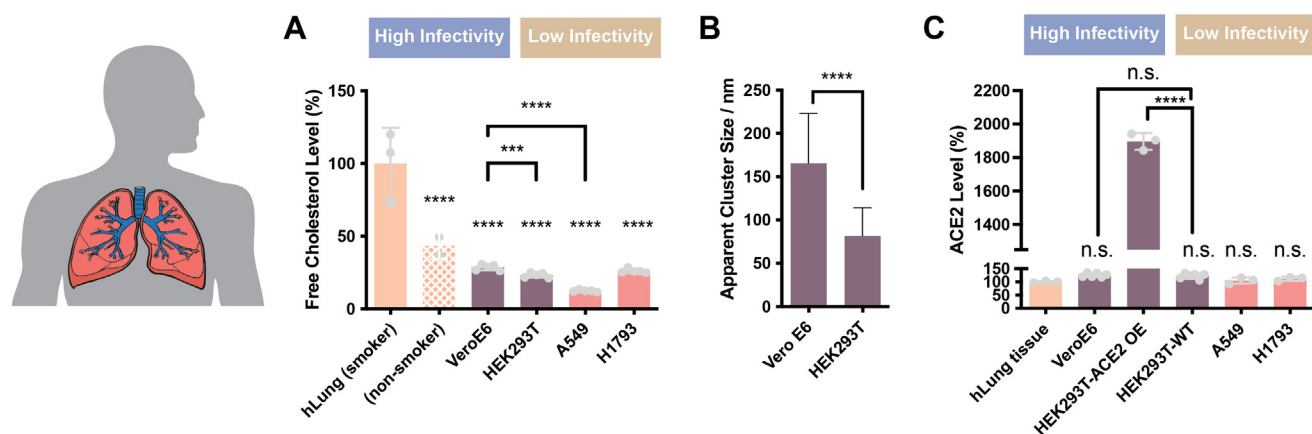
Figure 4. Tissue cholesterol, not ACE2 protein, correlates with cellular infectivity. *A*, free cholesterol from human lung tissue (epithelial airway; *orange*, from three smokers and two nonsmokers, including a patient with bronchitis and a healthy control) is compared with cultured cells, including kidney cell lines (*purple*) VeroE6 and HEK293T, lung cell lines (*red*) A549 and H1793, macrophage cell line RAW264.7 (*cyan*), and neuroblastoma 2a (N2a) cells. *B*, comparison of GM1 lipid clusters size in VeroE6 *versus* HEK293 cells using superresolution imaging. GM1 clusters were labeled with fluorescent cholera toxin B. *C*, ACE2 protein expression, measured by ELISA, does not correlate with infectivity. ACE2 protein levels in human lung tissue and veroE6 cells is low but their infectivity is high. Data are expressed as mean ± SD, ***$p < 0.001$, ****$p < 0.0001$, one-way ANOVA.

the reduced affinity for ACE2 would be less detrimental to viral entry. Alternatively, enhanced binding could decrease shedding of ACE2 near GM1 lipids (56).

A proposed model for cholesterol's role in age- and disease-dependent infection of SARS-CoV-2 is shown in Figure 3F. When cholesterol and saturated fat levels are low (in the case of children), ACE2 is primarily associated with PIP$_2$ clusters in the disordered region of the membrane. With age, average cholesterol levels in the lung increases and ACE2 shifts to GM1 lipids. In chronically ill patients, cellular cholesterol levels increase dramatically, further shifting ACE2 to GM1 entry points. The model is supported by age-dependent loading of cholesterol into lung tissue of mice (Fig. 3, *A* and *B*), translocation of ACE2 from PIP$_2$ domains to GM1 clusters, and increased size of GM1 clusters (Figs. 1C and 2F). Many proteins involved in the virulence of SARS-CoV-2 likely work this way, including priming of the spike protein by furin (see Fig. 5F) and perhaps even cholesterol-dependent proteins in the virion (49).

The cholesterol levels a protein experience could be affected by the location of the cholesterol. Cholesterol is thought to be higher in the extracellular leaflet (57, 58). This would decrease the affinity of palmitoylated proteins to GM1 lipids located on the inner leaflet and increase the association of GPI-linked proteins with GM1 lipids on the outer leaflet. Allowing the cholesterol to flip back to the inner leaflet could then act as a signal (59, 60) without the overall concentration in the membrane changing appreciably.

Lastly, very little is known about viral entry when ACE2 is bound to PIP$_2$. PIP$_2$ is localized to disordered lipids on the surface apart from endocytic lipids. Presumably when ACE2 is bound to PIP$_2$ the virus is cut by TMPRSS2 on the surface (61), but recent studies suggest this is likely still through the endocytic pathway (15, 19, 20, 62). Whether PIP$_2$ is the main site for surface cleavage or simply a factor that opposes endocytic entry will require future studies.

Cholesterol was found to be high in most monocytes of severe cases of COVID-19 while serum cholesterol from the same individuals was low (63). The high cholesterol in monocytes is consistent with cholesterol loading into tissue during chronic inflammation and suggests serum cholesterol may not always correlate with tissue cholesterol. Since we measured free cholesterol in the tissue, we expect a result similar to the monocytes, not serum.

ACE2's association with PIP$_2$ lipid domains is very similar to our previous finding with phospholipase D2. PIP$_2$ opposes the function of GM1 clusters (26, 64). These results suggest that cholesterol is likely in balance with PIP$_2$ in the membrane to regulate the trafficking of ACE2 in or out of the GM1 clusters and this may change with age and disease.

A binding site for PIP$_2$ within ACE2 protein is not known. However, the amino acid sequence of ACE2 shows a highly basic patch of ammino acids in the C terminus immediately proximal to the single transmembrane helix. PIP$_2$ is typically located on the inner leaflet of the membrane. A recent cryo-EM structure of full-length ACE2 in complex with the amino acid transporter sodium-dependent neutral amino acid transporter B^{0}AT1 has a bound phosphatic acid lipid (65), which is near the polybasic site (Figs. 1D and S4A). The acyl chains of the lipid bind to B^{0}AT1 and may help facilitate a complex. If so, cholesterol-induced translocation of the ACE2 to GM1 could disrupt the complex.

The putative PIP$_2$ site shares sequence similarities to the PIP$_2$-binding site in inward rectifying potassium channel 2.2 (Kir2.2) (66, 67) (Fig. S4B). In the absence of PIP$_2$ the lysine residues that form the PIP$_2$ pocket in Kir2.2 are disordered. Presumably when PIP$_2$ is bound, similarly positioned lysines in ACE2 coordinate with the phosphates on the inositol ring. When PIP$_2$ is not bound other phospholipids likely compete for the site (42, 67, 68). Further structural and functional studies are needed to confirm the interactions.

Apart from SARS-CoV-2 viral entry in the target cells, cholesterol-dependent GM1 cluster integrity also appears to be important for viral production in the producer cells. During viral production, the spike protein of SARS-CoV-2 needs to be cleaved by furin to be infective. We found that furin's

enzymatic activity is also regulated by its GM1 cluster association. Cholesterol (apoE + serum) increased furin's pair correlation with GM1 clusters (Fig. 5A), a location that likely favors hydrolysis of the spike protein at the S1/S2 site and facilitates priming of the virus. Unloading cholesterol from the cells (apoE−serum or MβCD) dramatically decreased the percent of furin associated with GM1 clusters (Fig. 5, B and C).

A lack of furin priming has been shown to decrease viral entry (69). As expected, treating producer cells with furin inhibitor (25 μM) decreased infection to ∼50% (Fig. 5D). If furin priming is decreased with low cholesterol, we expect virion from low cholesterol to also produce less infectious virion. Fig. 5E shows depletion of cholesterol in producer cells yields a much weaker virion. The resultant viral entry into normal control target cells decreased by 50%, suggesting low cholesterol likely decreases priming of the virions (Fig. 5F). Treating target cells with furin inhibitor (25 μM) (Fig. 5D) did not inhibit viral entry, suggesting furin does not cut an unprimed virion in the target cell.

According to our model, drugs that disrupt GM1 clusters, or drugs that increase cholesterol efflux, likely help critically ill patients with COVID-19. We and others have shown that polyunsaturated fatty acids, anesthetics, and mechanical force oppose cholesterol signaling through GM1 clusters (25–27, 64). Drugs that inhibit cholesterol synthesis, including statins (52), could also be helpful, especially if taken over time to avoid early infectivity.

Experimental procedures

Cell culture

HEK293T cells and HEK293T cells overexpressing human ACE2 (hACE2) were grown in Dulbecco's modified Eagle's medium containing 10% FBS and 1% penicillin/streptomycin.
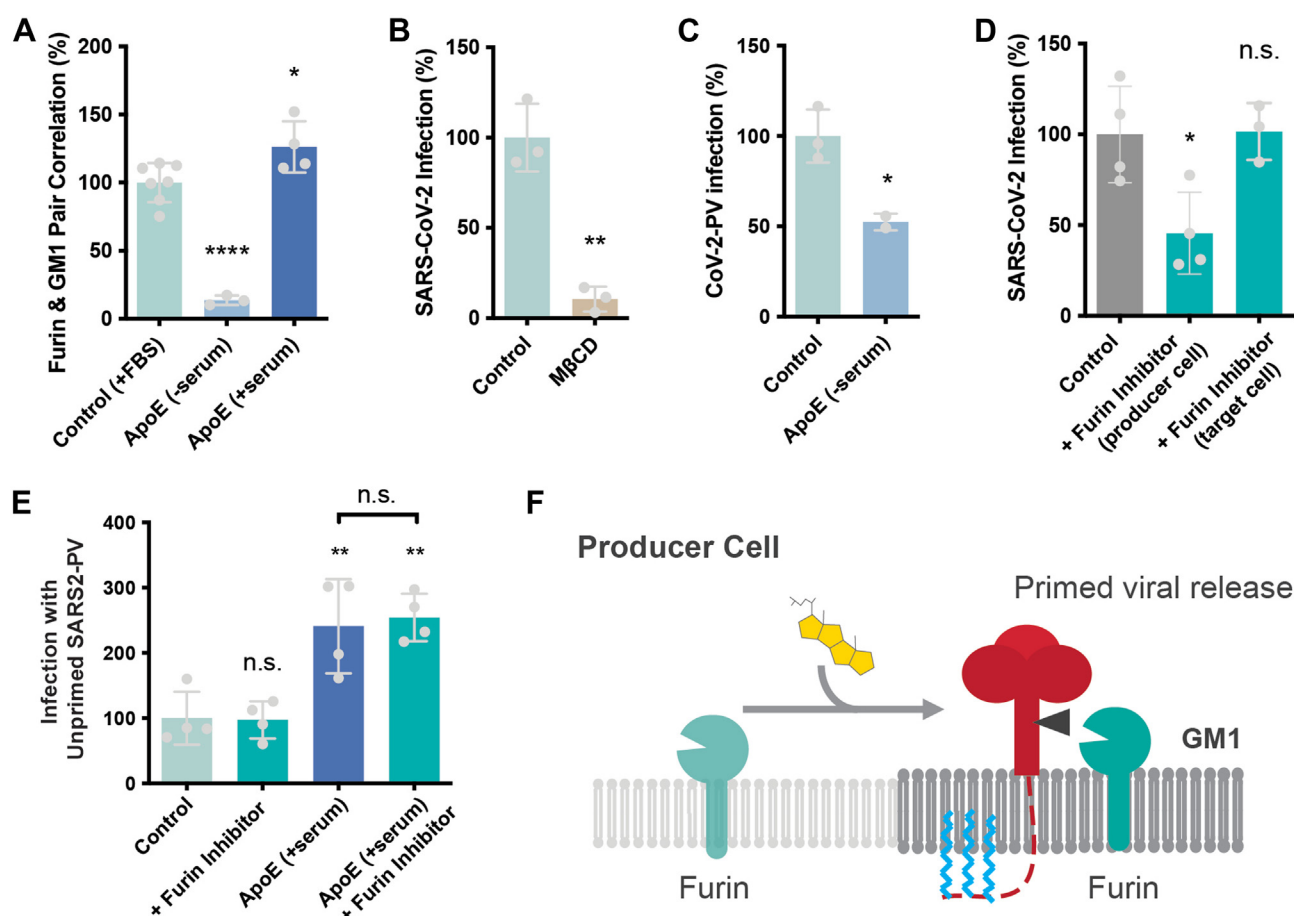

Figure 5. Cholesterol regulates furin processing in SARS-CoV-2 producer cells. *A*, furin localization to GM1 clusters is cholesterol dependent. Furin moves out of the GM1 cluster under low cholesterol condition (apoE extracts cholesterol from membrane). Cholesterol loading by apoE causes an increased furin GM1 lipid pair correlation. Data are expressed as mean ± SD, *$p < 0.05$, ****$p < 0.0001$, one-way ANOVA. *B*, cholesterol depletion by MβCD traffics furin out of the GM1 clusters into disordered region. Data are expressed as mean ± SD, **$p < 0.01$, two-sided Student's *t* test. *C*, cholesterol depletion with apoE in producer cells decreases the efficiency of viral entry by 50%, suggesting furin's cluster association is important for spike protein cleavage. Data are expressed as mean ± SD, *$p < 0.05$, two-sided Student's *t* test. *D*, furin inhibitor (25 μM) blocks S1/S2 cleavage and virion priming during SARS2-PV exit from producer cells, thus decreasing the efficiency for viral entry. Furin inhibitor treatment in target cells has no effect on viral entry; however, when the virus is produced in the presence of a furin inhibitor, infection decreases 50%. The result suggests furin cleavage during virus production increases SARS-CoV-2 viral entry. Data are expressed as mean ± SD, *$p < 0.05$, n.s. $p \geq 0.05$, one-way ANOVA. *E*, unprimed virion was produced in HEK293T cells with furin inhibitor and used to infect cells with and without furin inhibitor and with and without apoE. Furin inhibitor did not change the infectivity of the unprimed virion with or without cholesterol loading (apoE). Hence, furin appears unable to cut the virion in the target cell. Data are expressed as mean ± SD, **$p < 0.01$, n.s. $p \geq 0.05$, one-way ANOVA. *F*, speculative role of palmitoylation in SARS-CoV-2 priming of the spike protein. In high cholesterol furin moves from the disordered lipids (*light gray* lipids) to ordered GM1 lipids (GM1, *dark gray* lipids). Cholesterol-dependent membrane protein translocation is indicated by a *gray arrow* and the input of cholesterol (*yellow* shading).

HEK293T cells overexpressing hACE2 were generously provided by Dr Michael Farzan (Department of Immunology and Microbiology, Scripps Research). Cells were generated by transduction with murine leukemia virus (MLV) pseudotyped with the vesicular stomatitis virus G protein and expressing myc-hACE2-c9, as described (70). Briefly, HEK293T cells were cotransfected by PEI with three plasmids, pMLV-gag-pol, pCAGGS-VSV-G, and pQCXIP-myc-hACE2-c9, at a ratio of 3:2:1, and medium was refreshed after overnight incubation of transfection mix. The supernatant with produced virus was harvested 72 h post transfection and clarified by passing through 0.45-μm filter. 293T-hACE2 cells were selected and maintained with medium containing puromycin (Sigma). hACE2 expression was confirmed by SARS2-PV entry assays and by immunofluorescence staining using mouse monoclonal antibody recognizing c-Myc.

Production of SARS-CoV-2 pseudoviruses

Retroviruses pseudotyped with the SARS-CoV-2 spike proteins (SARS2-PV) were produced as described (71, 72) with modest modifications as described. HEK293T cells were transfected by X-tremeGENE 9 DNA Transfection Reagent (Millipore Sigma, #6365787001) at a ratio of 5:5:1 with a plasmid encoding MLV gag/pol proteins, a retroviral vector pQCXIX expressing firefly luciferase, and a plasmid expressing the spike protein of SARS-CoV-2 (GenBank YP_009724390) or a control plasmid (VSV-G). All the viral plasmids were provided by Dr Michael Farzan. Cell culture supernatant containing pseudovirus was harvested at 72 h post transfection. For furin inhibitor or apoE treatment, cells were incubated with 25 μM hexa-D-arginine amide (Furin Inhibitor II, Sigma-Aldrich, # SCP0148) or 4 μg/ml apoE (BioVision, #4696-500), respectively, over the process of viral production starting 6 h after transfection. Virus were then buffer exchanged with Amicon Ultra-4 Centrifugal Unit (Millipore Sigma, #UFC800396) to get rid of furin inhibitor in the media.

Viral entry assay

HEK293T cells were cultured in 96-well flat culture plates with transparent bottom (Corning Costar, #3585) precoated with poly-D-lysine. To provide a source of cholesterol to the apoE, we added 10% FBS, a common source of mammalian lipids, including ~310 μg/ml of cholesterol containing lipoproteins. ApoE can both load and unload cholesterol from cells (39, 73, 74). Importantly, apoE is not present in FBS (38). Cells were treated acutely (1 h) with 4 μg/ml of apoE, a physiologically relevant concentration (75).For MβCD treatment, cells were incubated with 100 μM MβCD for 30 min prior to virus infection. For furin inhibitor treatment, cells were incubated with 25 μM hexa-D-arginine amide for 1 h prior to and during the whole process of virus infection.

SARS-CoV-2 pseudoviruses were applied to the cells and allowed to infect at 37 °C for 24 h. After viral infection, efficiency of viral entry was determined through a firefly luciferase assay. Specifically, cells were washed with PBS once and 16 μl Cell Culture Lysis Reagent (Promega, #E153A) was added into each well. The plate was incubated for 15 min with rocking at room temperature. A volume of 8 μl of cell lysate from each well was added into a 384-well plate (Corning, #3574), followed by the addition of 16 μl of Luciferase Assay Substrate (Promega, #E151A). Luciferase activity measurement was performed on a Spark 20M multimode microplate reader (Tecan). All the infection experiments were performed in a biosafety level 2 laboratory.

dSTORM superresolution imaging

Fixed cell preparation

Cells were grown to 60% confluence. Cells were incubated with 4 μg/ml purified apoE protein with or without FBS supplementation (overnight) or 100 μM MβCD (30 min) in media. Cells were rinsed with PBS and then fixed with 3% paraformaldehyde and 0.1% glutaraldehyde for 20 min to fix both proteins and lipids. Fixative chemicals were reduced by incubating with 0.1% $NaBH_4$ for 7 min with shaking followed by three times 10-min washes with PBS. Cells were permeabilized with 0.2% Triton X-100 for 15 min and then blocked with a standard blocking buffer (10% bovine serum albumin [BSA]/ 0.05% Triton in PBS) for 90 min at room temperature. For labeling, cells were incubated with primary antibody (anti-ACE2 antibody [Abcam, #ab189168], anti-Furin antibody [Abcam, #ab3467], or anti-TMPRSS2 antibody [EPR3861] [Abcam, #ab92323]) for 60 min in 5% BSA/0.05% Triton/PBS at room temperature followed by five washes with 1% BSA/0.05% Triton/ PBS for 15 min each. Secondary antibody (donkey anti-rabbit cy3b and CTxB-647) was added in the same buffer as primary for 30 min at room temperature followed by five washes as stated above. Cells were then washed with PBS for 5 min. Cell labeling and washing steps were performed while shaking. Labeled cells were then postfixed with fixing solution, as above, for 10 min without shaking followed by three 5-min washes with PBS and two 3-min washes with deionized distilled water. Anti-ACE2 antibody (Abcam, #ab189168) was validated by Western blot in ACE2 knockout cells (see manufacture product page). Anti-TMPRSS2 antibodies were also verified by Western blots.

Lung tissue preparation

Lungs were removed from C57BL/6J wildtype and DIO mice. Housing, animal care, and experimental procedures were consistent with the Guide for the Care and Use of Laboratory Animals and approved by the Institutional Animal Care and Use Committee of the Scripps Research Institute. Mouse lung tissue slicing and staining were performed as described (76) with minor modifications. Mouse tissues were fixed in 4% paraformaldehyde/1% glutaraldehyde at 4 °C for 3 days. Tissues were sliced by the histology core. Sections (50 μm) were collected and placed into 24-well plates containing PBS. Fixative chemicals were reduced by incubating with 0.1% $NaBH_4$ for 30 min while gently shaking at room temperature followed by three times 10-min washes with PBS. Samples were permeabilized with 0.2% Triton X-100 for 2 h and then blocked with a standard blocking buffer (10% BSA/0.05% Triton in PBS) for 6 h at room temperature. For labeling, samples were incubated with primary

antibody for 3 h in 5% BSA/0.05% Triton/PBS at room temperature then 3 days at 4 °C followed by five washes with 1% BSA/0.05% Triton/PBS for 1 h each. Secondary antibody was added in the same buffer as primary for 3 days at 4 °C followed by five washes as stated above. Sample labeling and washing steps were performed while shaking. Labeled lung tissues were then postfixed with fixing solution, as above, for 1 h without shaking followed by three 30-min washes with PBS and two 30-min washes with deionized distilled water. Lung slices were mounted onto a 35-mm glass-bottom chamber (ibidi, #81158) and 2% agarose was pipetted onto the slice to form a permeable agarose pad and prevent sample movement during imaging.

dSTORM imaging

Images were recorded with a Zeiss ELYRA PS.1 microscope using TIRF mode equipped with a pil-immersion 63x objective. Andor iXon 897 EMCCD camera was used along with the Zen 10D software for image acquisition and processing. The TIRF mode in the dSTORM imaging provided low-background high-resolution images of the membrane. A total of 10,000 frames with an exposure time of 18 ms were collected for each acquisition. Excitation of the Alexa Fluor 647 dye was achieved using 642-nm lasers and that of Cy3B was achieved using 561-nm lasers. Cells and brain tissues were imaged in a photo-switching buffer comprising 1% β-mercaptoethanol (Sigma, #63689) and oxygen scavengers (glucose oxidase [Sigma, #G2133] and catalase [Sigma, #C40]) in 50 mM Tris (Affymetrix, #22638100) + 10 mM NaCl (Sigma, #S7653) + 10% glucose (Sigma, #G8270) at pH 8.0. Sample drift during acquisition was corrected by an autocorrelative algorithm.

For PIP2 imaging, images were recorded with a Bruker Vutara 352 with a 60X Olympus Silicone objective. Frames with an exposure time of 20 ms were collected for each acquisition. Excitation of the Alexa Fluor 647 dye was achieved using 640-nm lasers and that of Cy3B was achieved using 561-nm lasers. Laser power was set to provide isolated blinking of individual fluorophores. Cells were imaged in a photo-switching buffer comprising 1% β-mercaptoethanol (Sigma-Aldrich, #63689), 50 mM cysteamine (Sigma-Aldrich #30070), and oxygen scavengers (glucose oxidase [Sigma, #G2133] and catalase [Sigma, #C40]) in 50 mM Tris (Affymetrix, #22638100) + 10 mM NaCl (Sigma, #S7653) + 10% glucose (Sigma, #G8270) at pH 8.0. Axial sample drift was corrected during acquisition through the Vutara 352's vFocus system.

Images were constructed using the default modules in the Zen software. Each detected event was fitted to a 2D Gaussian distribution to determine the center of each point spread function plus the localization precision. The Zen software also has many rendering options including removing localization errors and outliers based on brightness and size of fluorescent signals. Pair correlation and cluster analysis was performed using the Statistical Analysis package in the Vutara SRX software. Pair Correlation analysis is a statistical method used to determine the strength of correlation between two objects by counting the number of points of probe 2 within a certain donut-radius of each point of probe 1. This allows for localization to be determined without overlapping pixels as done in traditional diffraction-limited microscopy. Cluster size estimation and cluster density were calculated through cluster analysis by measuring the length and density of the clusters comprising more than ten particles with a maximum particle distance of 0.1 μm. Ripley's H(r) analysis was performed to study the distribution of lipid clusters.

Live ACE2 activity assay

HEK293T cells were cultured in 96-well flat culture plates with transparent bottom (Corning Costar, #3585) precoated with poly-D-lysine. Cells were incubated with media containing 4 μg/ml apoE with or without FBS supplementation for 1 h before the assay. ACE2 activities were measured using ACE2 activity assay kit (BioVision, #K897-100) with modified protocol. Cells were washed with PBS once before incubation with assay buffer. A volume of 2 μl of ACE2 substrate was added to each well. For inhibitor treatment, 2 μl of ACE2 inhibitor (22 mM) was added to each well. The final volume was adjusted to 50 μl/well with ACE2 assay buffer. Fluorescent signals were measured in a kinetic mode for 2 h at 37 °C using a fluorescence microplate reader (Tecan Infinite 200 PRO, reading from bottom) with excitation wavelength of 320 nm and an emission wavelength of 420 nm. The endpoint values were then graphed (mean ± SD) and statistically analyzed (*t* test or one-way ANOVA) with GraphPad Prism software (v6.0f).

Lung cholesterol assay

To measure the relative changes in cholesterol level in lung tissue, we developed an Amplex Red–based cholesterol assay. Lungs were removed from C57BL/6J wildtype and DIO mice. Housing, animal care, and experimental procedures were consistent with the Guide for the Care and Use of Laboratory Animals and approved by the Institutional Animal Care and Use Committee of the Scripps Research Institute. The left lobe of each lung was homogenized with RIPA lysis buffer. After centrifugation, the supernatant was collected for cholesterol and protein measurement. A volume of 50 μl of supernatant was mixed with 50 μl of assay solution containing 100 μM Amplex red, 2 U/ml horseradish peroxidase, 4 U/ml cholesterol oxidase, and 4 U/ml cholesteryl esterase in PBS in 96-well plates with transparent bottom (Corning Costar, #3585). Relative cholesterol concentration was determined for each sample by measuring fluorescence activity with a fluorescence microplate reader (Tecan Spark, reading from bottom) with excitation wavelength of 530 nm and an emission wavelength of 585 nm. Subsequently, cholesterol level was normalized by tissue weights and protein concentration. Cholesterol signals were then graphed (mean ± SD) and statistically analyzed (one-way ANOVA) with GraphPad Prism software (v6.0f). A calibration curve was determined for known concentrations of cholesterol. The cholesterol added in dimethyl sulfoxide was incubated for 2 h and then read on Tecan Infinite 200 PRO at the same time as wt. mouse lung. The concentration of cholesterol was converted to μg/ml and normalized to the wet weight of the fixed lung tissue.

Statistical analyses

All statistical calculations were performed in GraphPad Prism v6.0. For the Student's t test, significance was calculated using a two-tailed unpaired parametric test with significance defined as $*p < 0.05$, $**p < 0.01$, $***p < 0.001$, $****p < 0.0001$. For the multiple comparison test, significance was calculated using an ordinary one-way ANOVA with Dunnett's multiple comparisons test.

Data availability

All data that support the findings of this study are available from the corresponding author upon request.

References

1. Wu, Z., and McGoogan, J. M. (2020) Characteristics of and important lessons from the coronavirus disease 2019 (COVID-19) outbreak in China: summary of a report of 72314 cases from the Chinese center for disease control and prevention. *JAMA* **323**, 13–16
2. Wu, J. T., Leung, K., Bushman, M., Kishore, N., Niehus, R., de Salazar, P. M., *et al.* (2020) Estimating clinical severity of COVID-19 from the transmission dynamics in Wuhan, China. *Nat. Med.* **26**, 506–510
3. Chu, J., Yang, N., Wei, Y., Yue, H., Zhang, F., Zhao, J., *et al.* (2020) Clinical characteristics of 54 medical staff with COVID-19: a retrospective study in a single center in Wuhan, China. *J. Med. Virol.* **92**, 807–813
4. Chen, T., Wu, D., Chen, H., Yan, W., Yang, D., Chen, G., *et al.* (2020) Clinical characteristics of 113 deceased patients with coronavirus disease 2019: retrospective study. *BMJ* **368**, m1091
5. Holly, J. M. P., Biernacka, K., Maskell, N., and Perks, C. M. (2020) Obesity, diabetes and COVID-19: an infectious disease spreading from the East Collides with the consequences of an unhealthy western lifestyle. *Front. Endocrinol. (Lausanne)* **11**, 1–13
6. Ruan, Q., Yang, K., Wang, W., Jiang, L., and Song, J. (2020) Clinical predictors of mortality due to COVID-19 based on an analysis of data of 150 patients from Wuhan, China. *Intensive Care Med.* **46**, 846–848
7. Li, W., Moore, M. J., Vasilieva, N., Sui, J., Wong, S. K., Berne, M. A., *et al.* (2003) Angiotensin-converting enzyme 2 is a functional receptor for the SARS coronavirus. *Nature* **426**, 450–454
8. Hoffmann, M., Kleine-Weber, H., Schroeder, S., Krüger, N., Herrler, T., Erichsen, S., *et al.* (2020) SARS-CoV-2 cell entry depends on ACE2 and TMPRSS2 and is blocked by a clinically proven protease inhibitor. *Cell* **181**, 271–280.e8
9. Glowacka, I., Bertram, S., Muller, M. A., Allen, P., Soilleux, E., Pfefferle, S., *et al.* (2011) Evidence that TMPRSS2 activates the severe acute respiratory syndrome coronavirus spike protein for membrane fusion and reduces viral control by the humoral immune response. *J. Virol.* **85**, 4122–4134
10. Matsuyama, S., Nagata, N., Shirato, K., Kawase, M., Takeda, M., and Taguchi, F. (2010) Efficient activation of the severe acute respiratory syndrome coronavirus spike protein by the transmembrane protease TMPRSS2. *J. Virol.* **84**, 12658–12664
11. Shulla, A., Heald-Sargent, T., Subramanya, G., Zhao, J., Perlman, S., and Gallagher, T. (2011) A transmembrane serine protease is linked to the severe acute respiratory syndrome coronavirus receptor and activates virus entry. *J. Virol.* **85**, 873–882
12. Lingwood, D., and Simons, K. (2010) Lipid rafts as a membrane-organizing principle. *Science* **327**, 46–50
13. Li, G. M., Li, Y. G., Yamate, M., Li, S. M., and Ikuta, K. (2007) Lipid rafts play an important role in the early stage of severe acute respiratory syndrome-coronavirus life cycle. *Microbes Infect.* **9**, 96–102
14. Lu, Y., Liu, D. X., and Tam, J. P. (2008) Lipid rafts are involved in SARS-CoV entry into Vero E6 cells. *Biochem. Biophys. Res. Commun.* **369**, 344–349
15. Bayati, A., Kumar, R., Francis, V., and McPherson, P. S. (2021) SARS-CoV-2 infects cells after viral entry via clathrin-mediated endocytosis. *J. Biol. Chem.* **296**, 1–12
16. Glebov, O. O. (2020) Understanding SARS-CoV-2 endocytosis for COVID-19 drug repurposing. *FEBS J.* **287**, 3664–3671
17. Yuan, Z., Pavel, M. A., Wang, H., Kwachukwu, J. C., Mediouni, S., Jablonski, J. A., *et al.* (2022) Hydroxychloroquine blocks SARS-CoV-2 entry into the endocytic pathway in mammalian cell culture. *Commun. Biol.* **5**, 958
18. Yuan, Z., and Hansen, S. B. (2023) Cholesterol regulation of membrane proteins revealed by two-color super-resolution imaging. *Membranes (Basel)* **13**, 250
19. Miao, L., Yan, C., Chen, Y., Zhou, W., Zhou, X., Qiao, Q., *et al.* (2023) SIM imaging resolves endocytosis of SARS-CoV-2 spike RBD in living cells. *Cell Chem. Biol.* **30**, 248–260.e4
20. Hansen, S. B., and Yuan, Z. (2023) Getting in on the action: new tools to see SARS-CoV-2 infect a cell. *Cell Chem. Biol.* **30**, 233–234
21. Syed, A. M., Ciling, A., Taha, T. Y., Chen, I. P., Khalid, M. M., Sreekumar, B., *et al.* (2022) Omicron mutations enhance infectivity and reduce antibody neutralization of SARS-CoV-2 virus-like particles. *Proc. Natl. Acad. Sci. U. S. A.* **119**, 1–7
22. Chen, J., Wang, R., Gilby, N. B., and Wei, G. W. (2022) Omicron variant (B.1.1.529): infectivity, vaccine breakthrough, and antibody resistance. *J. Chem. Inf. Model.* **62**, 412–422

ASBMB

23. Meng, B., Abdullahi, A., Ferreira, I. A. T. M., Goonawardane, N., Saito, A., Kimura, I., *et al.* (2022) Altered TMPRSS2 usage by SARS-CoV-2 Omicron impacts infectivity and fusogenicity. *Nature* **603**, 706–714

24. Levental, I., Lingwood, D., Grzybek, M., Coskun, U., and Simons, K. (2010) Palmitoylation regulates raft affinity for the majority of integral raft proteins. *Proc. Natl. Acad. Sci. U. S. A.* **107**, 22050–22054

25. [preprint] Petersen, E. N., Gudheti, M., Pavel, M. A., Murphy, K. R., Ja, W. W., Jorgensen, E. M., *et al.* (2019) Phospholipase D transduces force to TREK-1 channels in a biological membrane. *bioRxiv*. https://doi.org/10.1101/758896

26. Petersen, E. N., Chung, H.-W., Nayebosadri, A., and Hansen, S. B. (2016) Kinetic disruption of lipid rafts is a mechanosensor for phospholipase D. *Nat. Commun.* **7**, 13873

27. Pavel, M. A., Petersen, E. N., Wang, H., Lerner, R. A., and Hansen, S. B. (2020) Studies on the mechanism of general anesthesia. *Proc. Natl. Acad. Sci. U. S. A.* **117**, 13757–13766

28. Wang, H., Kulas, J. A., Wang, C., Holtzman, D. M., Ferris, H. A., and Hansen, S. B. (2021) Regulation of beta-amyloid production in neurons by astrocyte-derived cholesterol. *Proc. Natl. Acad. Sci. U. S. A.* **118**, e2102191118

29. Sieben, C., Sezgin, E., Eggeling, C., and Manley, S. (2020) Influenza a viruses use multivalent sialic acid clusters for cell binding and receptor activation. *Plos Pathog.* **16**, e1008656

30. Dou, X., Li, Y., Han, J., Zarlenga, D. S., Zhu, W., Ren, X., *et al.* (2018) Cholesterol of lipid rafts is a key determinant for entry and post-entry control of porcine rotavirus infection. *BMC Vet. Res.* **14**, 1–12

31. Glende, J., Schwegmann-Wessels, C., Al-Falah, M., Pfefferle, S., Qu, X., Deng, H., *et al.* (2008) Importance of cholesterol-rich membrane microdomains in the interaction of the S protein of SARS-coronavirus with the cellular receptor angiotensin-converting enzyme 2. *Virology* **381**, 215–221

32. Raut, P., Waters, H., Zimmerberg, J., Obeng, B., Gosse, J., and Hess, S. T. (2022) Localization-based super-resolution microscopy reveals relationship between SARS-CoV2 spike and phosphatidylinositol (4,5): biphosphate. *Proc. SPIE Int. Soc. Opt. Eng.* https://doi.org/10.1117/12.2613460

33. Betzig, E., Patterson, G. H., Sougrat, R., Lindwasser, O. W., Olenych, S., Bonifacino, J. S., *et al.* (2006) Imaging intracellular fluorescent proteins at nanometer resolution. *Science* **313**, 1642–1645

34. Hess, S. T., Girirajan, T. P. K. K., and Mason, M. D. (2006) Ultra-high resolution imaging by fluorescence photoactivation localization microscopy. *Biophys. J.* **91**, 4258–4272

35. Sahl, S. J., Hell, S. W., and Jakobs, S. (2017) Fluorescence nanoscopy in cell biology. *Nat. Rev. Mol. Cell Biol.* **18**, 685–701

36. Li, Z., Shue, F., Zhao, N., Shinohara, M., and Bu, G. (2020) APOE2: protective mechanism and therapeutic implications for Alzheimer's disease. *Mol. Neurodegener.* **15**, 1–19

37. Tall, A. R., and Yvan-Charvet, L. (2015) Cholesterol, inflammation and innate immunity. *Nat. Rev. Immunol.* **15**, 104–116

38. Varma, V. P., Devi, L., Venna, N. K., Murthy, C. L. N., Idris, M. M., and Goel, S. (2015) Ocular fluid as a replacement for serum in cell cryopreservation media. *PLoS One* **10**, 1–17

39. Luo, J., Yang, H., and Song, B. L. (2020) Mechanisms and regulation of cholesterol homeostasis. *Nat. Rev. Mol. Cell Biol.* **21**, 225–245

40. [preprint] Wang, H., Kulas, J. A., Higginbotham, H., Kovacs, M. A., Ferris, H. A., Scott, B., *et al.* (2022) Regulation of neuroinflammation by astrocyte-derived cholesterol. *bioRxiv*. https://doi.org/10.1101/2022.12.12.520161

41. Kuo, C.-L., Pilling, L. C., Atkins, J. L., Masoli, J. A. H., Delgado, J., Kuchel, G. A., *et al.* (2020) APOE e4 genotype predicts severe COVID-19 in the UK Biobank community cohort. *J. Gerontol. A Biol. Sci. Med. Sci.* **75**, 2231–2232

42. Chung, H.-W. W., Petersen, E. N., Cabanos, C., Murphy, K. R., Pavel, M. A., Hansen, A. S., *et al.* (2019) A Molecular target for an alcohol chain-length cutoff. *J. Mol. Biol.* **431**, 196–209

43. [preprint] Dicken, S. J., Murray, M. J., Thorne, L. G., Reuschl, A.-K., Forrest, C., Ganeshalingham, M., *et al.* (2021) Characterisation of B.1.1.7 and pangolin coronavirus spike provides insights on the evolutionary trajectory of SARS-CoV-2. *bioRxiv*. https://doi.org/10.1101/2021.03.22.436468

44. van den Bogaart, G., Meyenberg, K., Risselada, H. J., Amin, H., Willig, K. I., Hubrich, B. E., *et al.* (2011) Membrane protein sequestering by ionic protein-lipid interactions. *Nature* **479**, 552–555

45. Wang, J., and Richards, D. A. (2012) Segregation of PIP2 and PIP3 into distinct nanoscale regions within the plasma membrane. *Biol. Open* **1**, 857–862

46. Robinson, C. V., Rohacs, T., and Hansen, S. B. (2019) Tools for understanding nanoscale lipid regulation of ion channels. *Trends Biochem. Sci.* **44**, 795–806

47. Petersen, E. N., Pavel, M. A., Wang, H., and Hansen, S. B. (2020) Disruption of palmitate-mediated localization; a shared pathway of force and anesthetic activation of TREK-1 channels. *Biochim. Biophys. Acta Biomembr.* **1862**, 183091

48. Matsuyama, S., Nao, N., Shirato, K., Kawase, M., Saito, S., Takayama, I., *et al.* (2020) Enhanced isolation of SARS-CoV-2 by TMPRSS2-expressing cells. *Proc. Natl. Acad. Sci. U. S. A.* **117**, 7001–7003

49. Sanders, D. W., Jumper, C. C., Ackerman, P. J., Bracha, D., Donlic, A., Kim, H., *et al.* (2021) SARS-CoV-2 requires cholesterol for viral entry and pathological syncytia formation. *Elife* **10**, 1–47

50. Wang, C.-Y., and Liao, J. K. (2012) A mouse model of diet-induced obesity and insulin resistance. *Methods Mol. Biol.* **821**, 421–433

51. Daniels, L. B., Sitapati, A. M., Zhang, J., Zou, J., Bui, Q. M., Ren, J., *et al.* (2020) Relation of statin use prior to admission to severity and recovery among COVID-19 Inpatients. *Am. J. Cardiol.* **136**, 149–155

52. Wang, S., Li, W., Hui, H., Tiwari, S. K., Zhang, Q., Croker, B. A., *et al.* (2020) Cholesterol 25-Hydroxylase inhibits SARS-CoV-2 and coronaviruses by depleting membrane cholesterol. *EMBO J.* **39**, e106057

53. Mannar, D., Saville, J. W., Zhu, X., Srivastava, S. S., Berezuk, A. M., Tuttle, K. S., *et al.* (2022) SARS-CoV-2 Omicron variant: antibody evasion and cryo-EM structure of spike protein–ACE2 complex. *Science* **375**, 760–764

54. Cameroni, E., Bowen, J. E., Rosen, L. E., Saliba, C., Zepeda, S. K., Culap, K., *et al.* (2022) Broadly neutralizing antibodies overcome SARS-CoV-2 Omicron antigenic shift. *Nature* **602**, 664–670

55. Supasa, P., Ren, J., Stuart, D. I., Screaton, G. R., Zhou, D., Dejnirattisai, W., *et al.* (2021) Article Evidence of Escape of SARS-CoV-2 Variant B . 1 . 351 from Natural and Vaccine-Induced Sera. *Cell* **184**, 2348–2361.e6

56. Wang, J., Zhao, H., and An, Y. (2022) ACE2 shedding and the role in COVID-19. *Front. Cell. Infect. Microbiol.* **11**, 1–7

57. Pham, H., Singaram, I., Sun, J., Ralko, A., Puckett, M., Sharma, A., *et al.* (2022) Development of a novel spatiotemporal depletion system for cellular cholesterol. *J. Lipid Res.* **63**, 1–13

58. Buwaneka, P., Ralko, A., Liu, S. L., and Cho, W. (2021) Evaluation of the available cholesterol concentration in the inner leaflet of the plasma membrane of mammalian cells. *J. Lipid Res.* **62**, 1–18

59. Zhang, Y., Bulkley, D. P., Xin, Y., Roberts, K. J., Asarnow, D. E., Sharma, A., *et al.* (2018) Structural basis for cholesterol transport-like activity of the hedgehog receptor patched. *Cell* **175**, 1352–1364.e14

60. Liu, S.-L. L., Sheng, R., Jung, J. H., Wang, L., Stec, E., O'Connor, M. J., *et al.* (2017) Orthogonal lipid sensors identify transbilayer asymmetry of plasma membrane cholesterol. *Nat. Chem. Biol.* **13**, 268–274

61. Radzikowska, U., Ding, M., Tan, G., Zhakparov, D., Peng, Y., Wawrzyniak, P., *et al.* (2020) Distribution of ACE2, CD147, CD26, and other SARS-CoV-2 associated molecules in tissues and immune cells in health and in asthma, COPD, obesity, hypertension, and COVID-19 risk factors. *Allergy* **75**, 2829–2845

62. Kreutzberger, A. J. B., Sanyal, A., Saminathan, A., Bloyet, L.-M., Stumpf, S., Liu, Z., *et al.* (2022) SARS-CoV-2 requires acidic pH to infect cells. *Proc. Natl. Acad. Sci. U. S. A.* **119**, 1–12

63. Hu, X., Chen, D., Wu, L., He, G., and Ye, W. (2020) Low serum cholesterol level among patients with COVID-19 infection in Wenzhou, China. *SSRN Electron. J.* https://doi.org/10.2139/ssrn.3544826

64. Nayebosadri, A., Petersen, E. N., Cabanos, C., and Hansen, S. B. (2018) A membrane thickness sensor in TREK-1 channels transduces mechanical force. *SSRN Electron. J.* https://doi.org/10.2139/ssrn.3155650

65. Yan, R., Zhang, Y., Li, Y., Xia, L., Guo, Y., and Zhou, Q. (2020) Structural basis for the recognition of SARS-CoV-2 by full-length human ACE2. *Science* **367**, 1444–1448

66. Hansen, S. B., Tao, X., and MacKinnon, R. (2011) Structural basis of PIP2 activation of the classical inward rectifier K+ channel Kir2.2. *Nature* **477**, 495–498

67. Hansen, S. B. (2015) Lipid agonism: the PIP2 paradigm of ligand-gated ion channels. *Biochim. Biophys. Acta* **1851**, 620–628

68. Cabanos, C., Wang, M., Han, X., and Hansen, S. B. (2017) A soluble fluorescent binding assay reveals PIP2 antagonism of TREK-1 channels. *Cell Rep.* **20**, 1287–1294

69. Hoffmann, M., Kleine-Weber, H., and Pöhlmann, S. (2020) A Multibasic cleavage site in the spike protein of SARS-CoV-2 is Essential for infection of human lung cells. *Mol. Cell* **78**, 779–784.e5

70. Wicht, O., Burkard, C., de Haan, C. A. M., van Kuppeveld, F. J. M., Rottier, P. J. M., and Bosch, B. J. (2014) Identification and characterization of a proteolytically primed form of the murine coronavirus spike proteins after fusion with the target cell. *J. Virol.* **88**, 4943–4952

71. Moore, M. J., Dorfman, T., Li, W., Wong, S. K., Li, Y., Kuhn, J. H., *et al.* (2004) Retroviruses pseudotyped with the severe acute respiratory syndrome coronavirus spike protein efficiently infect cells expressing angiotensin-converting enzyme 2. *J. Virol.* **78**, 10628–10635

72. [preprint] Quinlan, B. D., Mou, H., Zhang, L., Guo, Y., He, W., Ojha, A., *et al.* (2020) The SARS-CoV-2 receptor-binding domain elicits a potent neutralizing resonse without antibody-dependent enhancement. *bioRxiv*. https://doi.org/10.1101/2020.04.10.036418

73. Chen, J., Zhang, X., Kusumo, H., Costa, L. G., and Guizzetti, M. (2013) Cholesterol efflux is differentially regulated in neurons and astrocytes: implications for brain cholesterol homeostasis. *Biochim. Biophys. Acta* **1831**, 263–275

74. Hayashi, H., Campenot, R. B., Vance, D. E., and Vance, J. E. (2007) Apolipoprotein E-containing lipoproteins protect neurons from apoptosis via a signaling pathway involving low-density lipoprotein receptor-related protein-1. *J. Neurosci.* **27**, 1933–1941

75. Lindh, M., Blomberg, M., Jensen, M., Basun, H., Lannfelt, L., Engvall, B., *et al.* (1997) Cerebrospinal fluid apolipoprotein E (apoE) levels in Alzheimer's disease patients are increased at follow up and show a correlation with levels of tau protein. *Neurosci. Lett.* **229**, 85–88

76. Licciulli, S., Avila, J. L., Hanlon, L., Troutman, S., Cesaroni, M., Kota, S., *et al.* (2013) Notch1 is required for Kras-induced lung adenocarcinoma and controls tumor cell survival via p53. *Cancer Res.* **73**, 5974–5984